Phase-contrast imaging with laser-plasma-accelerator betatron sources

J. van Tilborg[a], T. Ostermayr[a], H.-E. Tsai[a], T. Schenkel[a], C. G. R. Geddes[a], C. Schroeder[a], and E. Esarey[a]

[a]Lawrence Berkeley National Laboratory, Berkeley, California 94720, USA

ABSTRACT

Laser-plasma accelerators (LPAs) are known to intrinsically produce broad-bandwidth X-rays through the transverse motion of the accelerated electrons in the plasma wakefield. Due to the compact dimensions of the wakefield structure, this motion results in betatron radiation emission from a small point-like source (of order 1 μm in transverse size). Such a small source size enables high spatial resolution single-shot phase-contrast imaging, even for broad photon-energy spreads, simply by propagating the X-rays through a sample and onto a two-dimensional detector. In this manuscript we study, through simulations, the possibility to extend the resolution to the sub-micron regime. We find that the optimum geometry for <15 keV photons demands short (few-mm) drifts from source-to-sample, a photon flux of order 10^9 photons/shot, and the necessity to take the longitudinal source dimension into consideration. The presented framework behind the simulations will guide future betatron source development. The same expressions are also valid for other point-like LPA radiation sources such as Thomson- and Compton-scattered radiation.

Keywords: X-rays, compact light sources, laser-plasma acceleration, phase-contrast imaging

1. INTRODUCTION

Betatron motion of electrons inside the laser-plasma accelerator,[1] resulting in the emission of betatron X-rays, has been extensively reported on in high-profile papers over recent years.[2–11] The betatron spectrum has an intrinsically broad bandwidth, extending up to the critical photon energy E_c, before dropping off exponentially. E_c scales[3] with the electron Lorentz factor γ, the plasma density n_0, and the transverse beam size r_b, as $E_c[eV] = 5\times10^{-21}\gamma^2 n_0[\mathrm{cm}^{-3}]r_b[\mu\mathrm{m}]$. Betatron photon fluxes of over 10^{10} photons per shot have been recorded,[9] strongly depending on the laser, plasma, and electron injection parameters. Phase contrast imaging of LPA betatron emission is one of the key promising applications. This is due to the few-femtosecond pulse duration of the LPA electrons and betatron photons, the strong single-shot fluxes, but also the small μm-size transverse size of the betatron source. Phase-contrast imaging, performed in a lens-free and optics-free setup (drift from source to sample, and from sample to detector), carries a high degree of spatial coherence due to this small source size. This has resulted in milestone demonstrations of single-shot few-fs LPA betatron imaging of biological, medical, and dense matter structures, at few-μm spatial resolution.[8,9,11]

In this manuscript we will explore through simulations the possibility of enhancing the spatial resolution capabilities of LPA betatron phase-contrast imaging systems to sub-μm. This is of specific interest to bio-imaging, where macro-molecules or clusters can be as large as several 100s of nm. In terms of overcoming one key condition for sub-micron resolution imaging, namely the transverse source size, there have been measurements that supported such capabilities. For example, Ref. [6] mentioned a 0.1 μm betatron source size, while Ref. [12] presented the electron beam itself to have a transverse source size of 0.6 μm. Furthermore, simulations predict two-pulse two-color optical injection techniques can deliver small source size electron beam.[13] To address the geometrical and photon-flux considerations for sub-micron resolution imaging, we developed a simulation framework for phase-contrast imaging based on analytical expressions presented in Ref. [14] and citations therein. While our expressions are valid for an arbitrary photon energy distribution, we will use a 0-15 keV source as example, easily achievable with an LPA electron beam energy of order 200 MeV. The role of the phase-contrast setup geometry,

Correspondence: JvanTilborg@lbl.gov

International Conference on X-Ray Lasers 2020, edited by Davide Bleiner,
Proc. of SPIE Vol. 11886, 118860Q · © 2021 SPIE · CCC code:
0277-786X/21/$21 · doi: 10.1117/12.2592437

the photon energy spread, resolution, and longitudinal source size will be presented, providing the framework for others to tailor their betatron imaging model to their specific available parameters. Note that the same set of equations presented here are also valid for another point-like LPA radiation source, namely Thomson-scattered radiation (also referred to as Compton-scattered radiation), where the compact electron beam interacts with a counter-propagating laser pulse to radiate well-directed high-flux hard X-rays.[15–18]

2. SIMULATION FRAMEWORK

In this manuscript, an arbitrary energy distribution $f(\hbar\omega)$ of photon energy $\hbar\omega$ will be considered as photon source. The number of photons $dN/d(\hbar\omega)$ per energy band $d(\hbar\omega)$ can be calculated through $dN/d(\hbar\omega) = f(\hbar\omega)/(\hbar\omega)$. The total number of photons N_ϕ in the beam can be found by integrating $dN/d(\hbar\omega)$ over the radiation spectrum, namely $N_\phi = \int_{\hbar\omega} d(\hbar\omega) f(\hbar\omega)/(\hbar\omega)$. However, it can be desirable, especially for broad-bandwidth photon sources, to express the radiation pulse in terms of an equivalent photon number at fixed photon energy. For example, the photon energy distribution will have a mean energy, a median energy, or a critical energy E_c, and the photon pulse can thus be expressed in terms of number of photons of that energy. In case of using the mean energy, the equivalent photon count $N_{\phi,\text{mean}}$ can be found through $N_{\phi,\text{mean}} = \int_{\hbar\omega} f(\hbar\omega) d(\hbar\omega)/(\hbar\omega_{\text{mean}})$, with $(\hbar\omega_{\text{mean}}) = \int f(\hbar\omega) d(\hbar\omega)(\hbar\omega)/\int f(\hbar\omega) d(\hbar\omega)$.

In order the simulate or predict the single-shot X-ray image in the source-drift-sample-drift-detector geometry, at first mono-chromatic photons of photon energy $\hbar\omega$ are considered, yielding the image contribution at that energy. Then, the image composition from the full spectral distribution of the photon source will be stitched together.

We start by presenting an expression for the sample. The index of refraction of any material can be expressed as $n(\hbar\omega) = 1 - \delta(\hbar\omega) + \imath\beta(\hbar\omega)$, with δ the real part defining the phase velocity and phase accumulation, and β the imaginary part representing sample absorption. We will treat the photon beam as propagating in the z direction, and the sample as having a three-dimensional index of refraction distribution $n(x, y, z)$. For simplicity, the sample is assumed to be thin along z (like a film, foil, droplet, or virus particle). Following Ref. [14], the sample can thus be approximated as a two-dimensional structure, positioned at $z = 0$, inflicting a correction to the incoming electric field profile $E_{\text{in}}(x, y)$ of

$$E_{\text{out}}(x, y, \hbar\omega) = E_{\text{in}}(x, y, \hbar\omega) \exp\left(-\imath \int_{z'} \delta(x, y, z', \hbar\omega) \frac{2\pi}{\lambda} dz'\right) \exp\left(-\int_{z'} \beta(x, y, z', \hbar\omega) \frac{2\pi}{\lambda} dz'\right), \tag{1}$$

with $\lambda = 2\pi c/\omega$ the photon wavelength, and where integration along z' accounts for projection of the three-dimensional sample on the two-dimensional (x, y) plane.

As an arbitrary example of a potential sample, we propose to represent the sample as an ensemble of uniform spheres (such as several virus particles/spheres inside a water droplet/sphere), with each sphere m having a radius R_m, centroid location (x_m, y_m, z_m), and material index $\delta_m(\hbar\omega)$ and $\beta_m(\hbar\omega)$. In case there is an overlap between two spheres (as is the case for a virus particle inside a water droplet), the index of refraction of the smaller volume (the virus particle) should be defined as relative to the larger volume (the droplet). Geometrical consideration yields that the z-integrated thickness of each sphere is $2\sqrt{R_m^2 - (x - x_m)^2 - (y - y_m)^2}$. The spatial electric field distribution $E_{\text{out}}(x, y, \hbar\omega)$ of the photon beam at the sample exit can then be derived from Eq. (1) to be $E_{\text{out}}(x, y, \hbar\omega) = E_{\text{in}}(x, y, \hbar\omega) \exp\left[-\imath\Phi(x, y, \hbar\omega)\right]$, with

$$\Phi(x, y, \hbar\omega) = \sum_m 2\sqrt{R_m^2 - (x - x_m)^2 - (y - y_m)^2} \frac{2\pi}{\lambda} \left[\delta_m(\hbar\omega) - \imath\beta_m(\hbar\omega)\right]. \tag{2}$$

The next step is to calculate how this field profile $E_{\text{out}}(x, y, \hbar\omega)$ at the sample exit plane $z = 0$ propagates from the sample to the detector plane at distance R_2, yielding $E_{\text{detector}}(x, y, R_1, R_2, \hbar\omega)$, with the distance from the point source to the sample labeled as R_1, see Fig. 1. Again we will follow the approach presented by Ref. [14], where, accounting for the (point)source-sample-detector geometry, the effective propagation distance from sample to detector is not R_2, but is defined as $z_{\text{eff}} = (R_1 R_2)/(R_1 + R_2)$. In fact, for common geometries where $R_2 \gg R_1$, one can find that $z_{\text{eff}} \approx R_1$. For example, when the detector is placed R_2 =2 meter from the sample, the effective

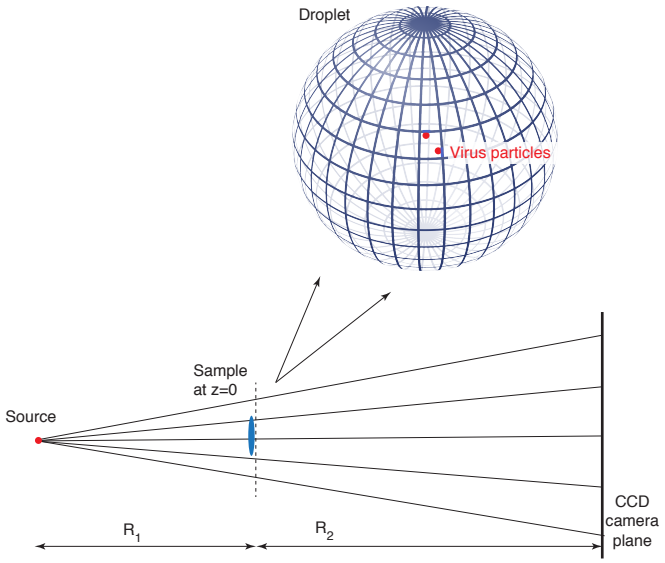

Figure 1. Schematic of the phase-contrast imaging geometry. The photon source is considered to be a point-like source of transverse size σ_s, positioned at distance R_1 from the sample. The sample is placed at $z = 0$, with the detector plane at distance R_2 from the sample. To account for the diverging photon source geometry, it was derived[14] that the effective propagation distance from the sample to the detector can be expressed as $z_{\text{eff}} = (R_1R_2)/(R_1 + R_2)$, which can be approximated by $z_{\text{eff}} \simeq R_1$ for geometries where R_2 is large.

propagation distance z_{eff} to be used is only $z_{\text{eff}} = 9.95$ mm for a betatron point source R_1 =10 mm upstream of the sample. We will also follow the approach of switching from the transverse coordinates (x, y) to the transverse spatial frequencies (u, v). The spatial Fourier transform of $E_{\text{out}}(x, y, \hbar\omega)$ at the sample exit plane will thus be rewritten as $\widetilde{E}_{\text{out}}(u, v, \hbar\omega)$. In the spatial frequency space, propagation over a distance of z_{eff} is best aided through introduction of a variable $\chi(R_1, R_2) = \pi\lambda z_{\text{eff}}(u^2 + v^2) = \pi\lambda R_1R_2(u^2 + v^2)/(R_1 + R_2)$. The field distribution at the detector plane R_2, in the spatial-frequency domain, can be derived to be[14,19]

$$\widetilde{E}_{\text{detector}}(u, v, R_1, R_2, \hbar\omega) = \exp\left[\frac{i2\pi R_1R_2}{\lambda(R_1 + R_2)}\right] \exp\left[\imath\chi(R_1, R_2)\right]\widetilde{E}_{\text{out}}(u, v, \hbar\omega)g_{\text{source}}(u, v), \tag{3}$$

with $g_{\text{source}}(u, v)$ incorporating the effect of a non-zero transverse source size of the photon beam. The finite source size σ_s will result in spatial frequencies $(u, v) > \sigma_s^{-1}$ at the sample to be washed out, resulting in loss of signal and loss of resolution. For a Gaussian distribution of the transverse photon source with size σ_s, we can calculate the cut-off spectral source-size function $g_{\text{source}}(u, v)$ to be

$$g_{\text{source}}(u, v) = \exp\left[-\pi^2\sigma_s^2(u^2 + v^2)\right]. \tag{4}$$

Note that the field distribution at R_2 in absence of a sample ($\delta_m \to 0,\ \beta_m \to 0,\ \sigma_s \to 0$), is

$$\widetilde{E}_{\text{detector},0}(u, v, R_1, R_2, \hbar\omega) = \exp\left[\frac{i2\pi R_1R_2}{\lambda(R_1 + R_2)}\right] \exp\left[\imath\chi(R_1, R_2)\right]\widetilde{E}_{\text{in}}(u, v, \hbar\omega). \tag{5}$$

At detector plane R_2, the spatial distribution of the electric field can be calculated[14] to be $E_{\text{detector}}(X, Y, R_1, R_2, \hbar\omega)$, which is simply the inverse Fourier transform of $\widetilde{E}_{\text{detector}}(u, v, R_1, R_2, \hbar\omega)$ followed by replacing (x, y) with (X, Y), defined as $X = xR_2/R_1$ and $Y = yR_2/R_1$, to account for the sample-to-detector magnification R_2/R_1. The intensity distribution at the detector plane is defined as $I_{\text{detector}}(X, Y, R_1, R_2, \hbar\omega) = |E_{\text{detector}}(X, Y, R_1, R_2, \hbar\omega)|^2$. Similarly, the sample-out intensity distribution is $I_{\text{detector},0}(X, Y, R_1, R_2, \hbar\omega) = |E_{\text{detector},0}X, Y, R_1, R_2, \hbar\omega)|^2$.

To turn the intensity distribution $I_{\text{detector}}(X, Y, R_1, R_2, \hbar\omega)$ into a photon number distribution $d^3I_{\text{N,detector}}(X, Y, \hbar\omega)/d(\hbar\omega)dXdY$, we want to ensure that the total number of photons in the photon energy band $d(\hbar\omega)$ in the sample-out case matches the photon number at the source $dN/d(\hbar\omega)$. The corrected spatial distribution at the detector, in units of number of photons per area $dXdY$ per bandwidth $d(\hbar\omega)$, can thus be expressed as

$$\frac{d^3I_{\text{N,detector}}(X, Y, \hbar\omega)}{d(\hbar\omega)dXdY} = \frac{dN}{d(\hbar\omega)} \frac{I_{\text{detector}}(X, Y, R_1, R_2, \hbar\omega)}{\iint_{-\infty}^{\infty} dX'dY' I_{\text{detector},0}(X', Y', R_1, R_2, \hbar\omega)}. \tag{6}$$

For laser-plasma-driven betatron sources, we now include one level of complexity, namely the fact that the emission source is better represented as a line of length L, rather than a point-like source. For example, the emission could occur over several betatron periods inside the plasma. This effect has been commented on in recent manuscripts, such as Ref. [10], but no quantative description has been provided to this point. As a simplified model, we approximate this effect by considering the betatron source to be M discrete emission point sources lined up in a row, each with distance $R_{1,M}$ from the sample, and each with photon flux distribution $dN_M/d(\hbar\omega)$ such that $\sum_M dN_M/d(\hbar\omega) = dN/d(\hbar\omega)$. In this case, the spatial photon distribution at the detector, following Eq. (6), becomes

$$\frac{d^3I_{\text{N,detector}}(X, Y, \hbar\omega)}{d(\hbar\omega)dXdY} = \sum_M \frac{dN_M}{d(\hbar\omega)} \frac{I_{\text{detector}}(X, Y, R_{1,M}, R_2, \hbar\omega)}{\iint_{-\infty}^{\infty} dX'dY' I_{\text{detector},0}(X', Y', R_{1,M}, R_2, \hbar\omega)}. \tag{7}$$

Consideration of the longitudinal length L of the betatron source is important in the regime $L \sim R_1$, when there are considerable differences in the distance to the sample from the closest and the further betatron emission contributors.

The last step in this simulation framework description is the inclusion of the camera pixel dimension and photon statistics. The CCD camera has $N_x \times N_y$ pixels, with index (i, j), each with physical size ΔX and ΔY. This yields a a spatial axis calibration $X_i = \Delta X(i-1/2) - \Delta X N_x/2$ and $Y_j = \Delta Y(j-1/2) - \Delta Y N_y/2$. For each pixel (i, j), the spatial photon count distribution $d^3I_{\text{N,detector}}(X, Y, \hbar\omega)/d(\hbar\omega)dXdY$ should be integrated over dX following the limits $(X_i - \Delta X/2)$ to $(X_i + \Delta X/2)$, and over dY following the limits $(Y_j - \Delta Y/2)$ to $(Y_j + \Delta Y/2)$. The resulting spectrally-differentiated CCD flux distribution will be labeled as $dI_{\text{N,detector}}(X_i, Y_j, \hbar\omega)/d(\hbar\omega)$. The final steps are (1) to introduce a statistical noise[14] on every CCD camera pixel (i, j), (2) adding a wavelength-dependent conversion factor $C(\hbar\omega)$ from photon to CCD counts, and (3) to consider the photon beam over the full spectral distribution, which can be achieved by integrating $dI_{\text{N,detector}}(X_i, Y_j, \hbar\omega)/d(\hbar\omega)$ over the photon energies that are present. The noise is incorporated by adding or subtracting a photon correction number of $h_{\text{normal}} \times \sqrt{dI_{\text{N,detector}}(X_i, Y_j, \hbar\omega)/d(\hbar\omega)}$ for each pixel (i, j), with h_{normal} a randomly chosen value following the standard normal distribution of mean 0 and standard deviation 1. This results in the following expression for CCD counts per pixel

$$I_{\text{counts,detector}}(X_i, Y_j) = \int_{\hbar\omega} d(\hbar\omega) C(\hbar\omega) \left[\frac{dI_{\text{N,detector}}(X_i, Y_j, \hbar\omega)}{d(\hbar\omega)} + h_{\text{random}} \sqrt{\frac{dI_{\text{N,detector}}(X_i, Y_j, \hbar\omega)}{d(\hbar\omega)}} \right]. \tag{8}$$

A good intuitive picture can be obtained regarding the interplay between the spatial frequencies in the sample, the photon energy of incoming radiation, and the distances R_1 and R_2, by following the analysis of Refs. [14,19] in the weak-object approximation. It was derived there that the intensity contrast resulting from the real part of the index of refraction (the phase term) develops as $\sim \sin\chi$, where χ was previously introduced as $\chi = \pi\lambda(u^2 + v^2)R_1R_2/(R_1 + R_2)$. One can see that at $R_2 = 0 \rightarrow \sin\chi = 0$, highlighting that the phase imprint by the sample has not yet translated into an intensity variation. The maximum intensity contrast from the sample phase modulation occurs at $\chi = \pi/2$ (and additional integers of π), which in the regime $R_2 \gg R_1$ translates into an optimum sample source-sample separation of

$$R_1^{\text{opt}} = \frac{1}{2\lambda(u^2 + v^2)}. \tag{9}$$

Thus, if one aims to resolve a spatial feature of size σ, such that $(u^2 + v^2) \simeq 1/\sigma^2$, it can be derived that the ideal position from source to sample is $R_1^{\text{opt}} = \sigma^2/(2\lambda)$. For example, a $\sigma = 10$ μm feature would ideally require

$R_1^{\rm opt} = 12$ cm for 3 keV (λ=0.41 nm) and $R_1^{\rm opt}$=1.2 m for 30 keV (λ=0.041 nm) radiation. For a $\sigma = 1$ μm feature we retrieve an optimum $R_1^{\rm opt} = 0.12$ cm for 3 keV and $R_1^{\rm opt}$=1.2 cm for 30 keV photons. Note that the same analysis as above can be pursued for the imaginary index of refraction by the sample (yielding absorption), except that the intensity contrast now develops as $\sim \cos\chi$. As expected, already at $R_2 = 0$ (where $\chi = 0$) there is an immediate intensity modulation, and this maximum is repeated at integers of π. Keep in mind that a typical sample is made up of a wide range of spatial frequencies, and each spatial frequency is transformed into an intensity modulation at its own contrast transfer function (its own imaging efficiency).

3. SIMULATIONS

To provide insight into simulated betatron phase-contrast images, especially in the context of sub-micron resolution, we will consider a water droplet example containing two embedded virus particles. The water droplet is approximated as a uniform-density sphere of radius 20 μm, centered at $(x = 0, y = 0)$, with a tabulated X-ray index of refraction[20] of

$$\log_{10}(\delta_{\rm water}) = -3.0 - 2.1 \times \log_{10}(\hbar\omega_{\rm keV} - 2.7), \qquad \log_{10}(\beta_{\rm water}) = -3.2 - 3.7 \times \log_{10}(\hbar\omega_{\rm keV} - 2.7). \tag{10}$$

The two virus particles will be approximated as a uniform sphere of radius 200 nm, one centered at $(x = 0, y = 0)$ and the other at various separation distances, with the index of refraction being different from water by $\Delta\delta_{\rm virus}$ and $\Delta\beta_{\rm virus}$. For example, a water droplet with a virus particle that is optically identical to water would be accounted for as a uniform droplet of index $(\delta_{\rm water}, \beta_{\rm water})$ and a relative virus contribution of $\Delta\delta_{\rm virus} = \Delta\beta_{\rm virus} = 0$. For a virus particle with an index identical to vacuum (thus effectively equivalent to putting a vacuum bubble inside the droplet), we would use $\Delta\delta_{\rm virus} = -\delta_{\rm water}$ and $\Delta\beta_{\rm virus} = -\beta_{\rm water}$. In general terms, for a virus $\times p$ times as optically dense as water, we would define the ensemble as an uniform water droplet of $(\delta_{\rm water}, \beta_{\rm water})$ with superimposed virus particles of index of $\Delta\delta_{\rm virus} = (p-1)\delta_{\rm water}$ and $\Delta\beta_{\rm virus} = (p-1)\beta_{\rm water}$.

As an approximate LPA betatron imaging example, we will define the X-ray spectrum $f(\hbar\omega)$ to be peaked at 3 keV, with a Gaussian width of 5 keV (truncated at 0 keV), see the blue curves in the top row of Fig. 2. While the betatron spectrum, just like Thomson- or Compton-scattered radiation, could more accurately be described with a critical-energy-based synchrotron asymptotic limit spectrum,[5] our choice of Gaussian spectral approximation provides similar qualitative spectral features. In our example, loosely resembling betatron radiation from 200 MeV electrons and a LPA plasma density of 5×10^{18} cm^{-3}, the mean value of the photon flux is $(\hbar\omega_{\rm mean})$=5.4 keV. In units of 5.4 keV photons, the full betatron pulse contained 3.2×10^{10} such photons. The source size was defined as having a Gaussian width of $\sigma_s = 0.1$ μm. Embedded in the 20-μm-radius water sphere, the two 200-nm-radius virus spheres are separated horizontally by 0.7 μm, and are defined to have an index of refraction twice of water ($p = 2$). The CCD has pixels of 40 μm by 40 μm in size. The distance source-to-sample was chosen at $R_1 = 2$ mm, and the distance sample-to-detector at R_2=1 m, thus yielding a magnification of $R_2/R_1 = \times 500$. For simplicity, we used the photon-to-count conversion factor to be $C(\hbar\omega) = 1$, although one could easily expand this to a more realistic function including the manufacturer-supplied photon-to-counts conversion and the photon-capture quantum efficiency.

The simulation results are shown in Fig. 2, for individual spectral bands in plots (a), (b), and (c), and for the full spectrum in (d). For the choice of geometry and spectral distribution, and considering a flux of 3.2×10^{10} photons, we can observe that the sub-micron virus particles are well-observable, and well-distinguishable. The water sphere itself is dominated by the sharp gradients at its edge, and we can observe both diffraction effects as well as absorption [especially at <4 keV in Fig. 2(a)]. The virus particles are least sharp at the lower photon energies (as expected since $\chi \gg \pi/2$), while the amplitude- and phase-induced contrast in counts is stronger at such energies, as expected from Eq. (10). In fact, when the photon energy is too low, the phase-shift and absorption through the sample becomes so large that the overall transmission drops towards zero, forcing use of higher photon energies.

To examine the signal-to-noise contrast in the example shown in Fig. 2, we repeated the simulations at four levels of photon flux, expressed in units of 5.4-keV photons, namely 3.2×10^{11} photons in Fig. 3(a), 3.2×10^{10} photons in Fig. 3(b), 3.2×10^{9} photons in Fig. 3(c), and 3.2×10^{8} photons in Fig. 3(d). Based on the choice in drift distances and 25-mrad divergence, the number of photons inicident per per pixel varies from approximately

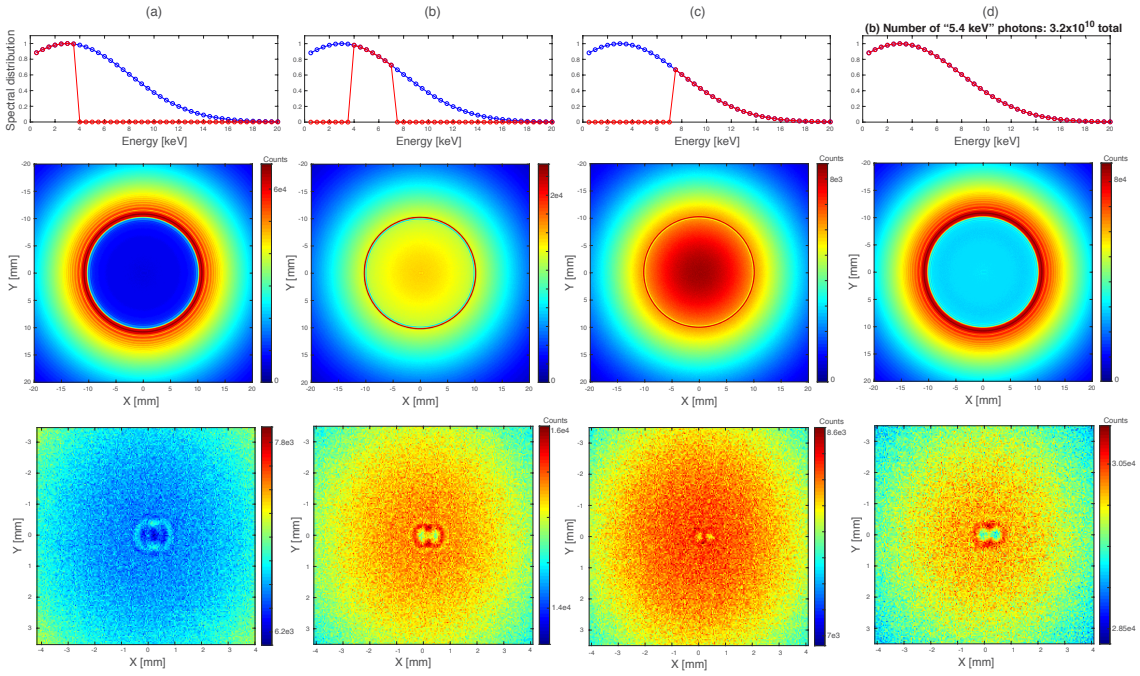

Figure 2. (a-d) Simulation results of a water droplet with two embedded virus particles being imaged onto a CCD camera. At a magnification of $R_2/R1 = \times 500$, the 20 μm radius water droplet will appear with diameter 10 mm. Figures (a), (b), and (c) show the image contribution of several segments of the photon spectrum (see red curves in top row), while Fig. (d) displays the full integrated image. The bottom row reveals the CCD counts per pixel for a zoomed-in area at 8x8mm (16x16 μm at the sample), showing the two virus particles. At higher photon energy the virus intensity imprint becomes weaker, but with better spatial resolution.

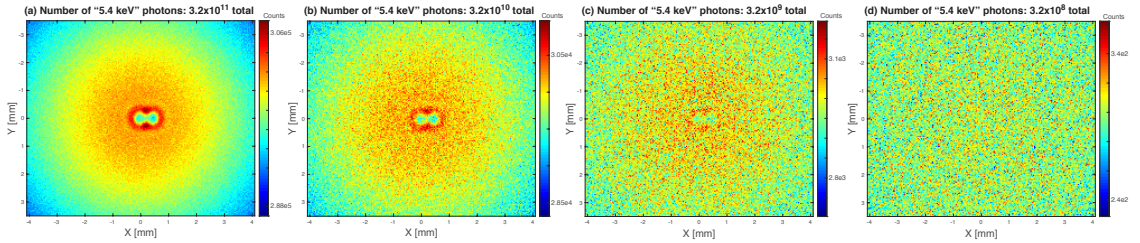

Figure 3. For the same simulation geometry of Fig. 2, this figure displays the simulated images for four different flux scenarios, expressed in units of 5.4-keV-equivalent photons: (a) 3.2×10^{11} photons, (b) 3.2×10^{10} photons, (c) 3.2×10^{9} photons, and (d) 3.2×10^{8} photons. In this example, once the flux drops to $< 10^9$ photons, the virus particles become hardly observable.

from 3×10^5 in (a) to 3×10^2 in (d). Already in Fig. 3(c) the two virus particle are barely visible, and they are buried in the noise at 3.2×10^8 photons in Fig. 3(d). A flux requirement of 10^9 photons in this energy range therefore seems like a reasonable detection threshold. Note that averaging or integrating of LPA betatron shots could be considered (for example 10^7 photons per shots integrated over 100 shots), but the stability of the source-sample-detector line would have to be actively stabilized. If any of these three components jitters beyond control (for example, the transverse source location jitters by 1 micron), the superposition of images would not yield the desired result.

As was introduced in Sec. 2, the LPA betatron source is intrinsically based on photons emitted by the electrons performing a transverse oscillation along a longitudinal path. With the betatron period of order 100 μm, and with typically several betatron periods contributing to the photon source, the longitudinal source line

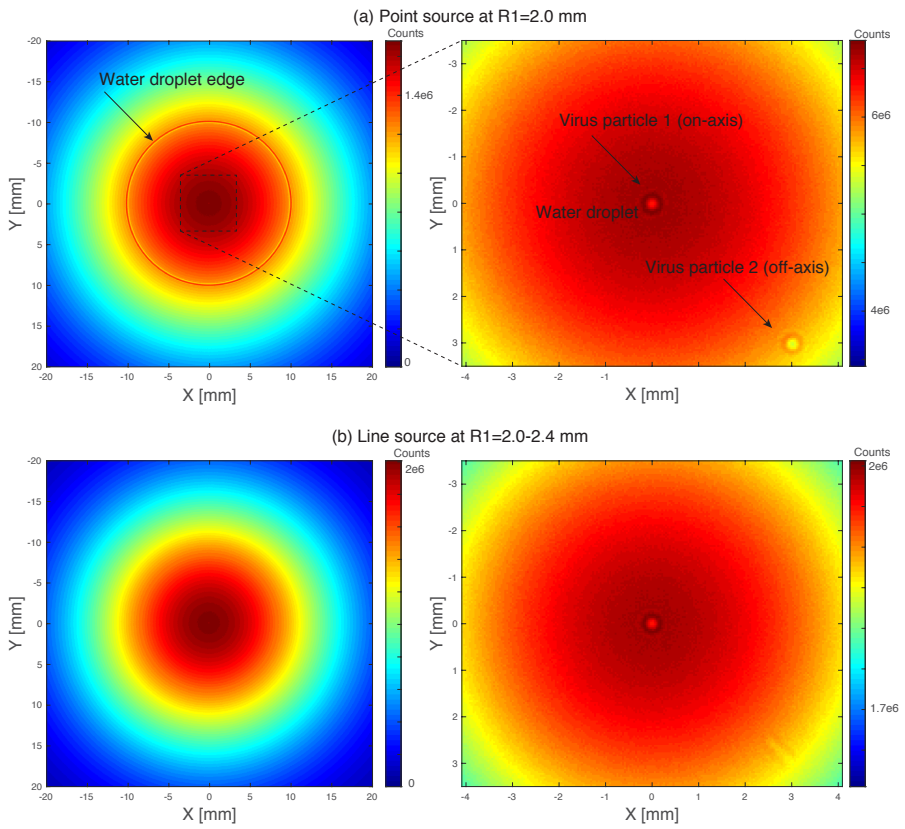

Figure 4. (a) Simulated detector count distribution for a mono-chromatic 15 keV photon source originating from a point source. The water sphere edges and two virus spheres are clearly observable, as expected from a 10^{12} photons/shot flux. (b) Detector distribution for the same photon flux, but now with the source distributed over a 0.4mm line source. The longitudinally extending photon source leads to radial streaking of off-axis features at the sample, such as the water sphere edge and the off-axis virus particle.

length could become relevant when of equal size to the distance source-to-sample R_1. To study the impact of the line source, we simplified the photon source to be a mono-chromatic source of 10^{12} photons at 15 keV. The same water sphere and virus particles as before are considered, except that the second virus particle will be positioned off-axis at $(x, y) = (6, 6)$ μm. Figure 4(a) displays the simulated detector image in the assumption of a point source at R_1=2 mm. As in previous figures, both the water sphere outline as well as the virus spheres are clearly observed. Figure 4(b) shows the same sample, but now with a photon source with a length of 0.4mm, extending from R_1=2.0 mm to 2.4mm. The integrated photon flux is kept the same. One can observe that while the on-axis virus particle remains unaffected, the off-axis one is smeared out into a streak pattern (pointing towards the origin). Also, the edge of the water sphere is no longer observable. We want to emphasize two contributors to these effects: (1) since there now is no singular distance R_1, the χ parameter that dictates contrast amplitude and spatial resolution is now different for the various R_1 components, resulting in a modified image. But more importantly, (2) the magnification R_2/R_1 will be different for the various source contributors, leading to a superposition of images each at their own magnification. It is important to note that not only is the projected size of each spatial feature a function of the varying ratio R_2/R_1, but also it' off-axis position on the detector plane (a x offset at the sample results in R_2/R_1 offset at the detector). This means that off-axis sample features will be smeared out, and streaked along the axis to the origin, as observed in Fig. 4(b).

4. CONCLUSION

In conclusion, in this manuscript we presented an overview of the equations that can be applied to model phase-contrast imaging with LPA betatron X-rays (see also Sect. 2-3 [21]). The role of the sample and detector placement, the photon spectrum, the transverse source size, the spatial frequencies making up the sample, the photon statistics on the detector camera, and the longitudinal extent of the photon source, were all considered. Simulations were carried out to highlight the approach and necessary parameters to realizing sub-micron spatial resolution.

The sub-micron imaging (in the simulation example presented here, made up of two 200-nm-radius virus particles inside a water droplet) demands a photon spectrum in the 5-10 keV range, and a source position R_1 only a few mm from the photon source. For these parameters, the photon flux should be at least of order 10^9 photons per image. Note that multi-shot integration and averaging can relax the betatron flux parameters, providing that fluctuations in transverse source location are kept at acceptable level. For multi-micron resolutions these requirements are significantly relaxed. It was also found that due to the short source-to-sample distance, the longitudinal extent of the photon source can lead to considerable image smearing effects, dependent on the off-axis location of the sample features.

The above considerations are aimed to help guide the choice of phase-contrast imaging geometry. Especially with the aim of achieving sub-micron resolution, the conceptual approach presented here can help define the specifications for novel LPA injection mechanisms as betatron source, such as two-pulse two-color ionization.[13] Note that the same conceptual framework presented here is also valid for other point-like LPA radiation sources such as Thomson- and Compton-scattered radiation.

ACKNOWLEDGMENTS

This work was supported by the U.S. Department of Energy (DOE) under Contract Numbers DE-AC02-05CH11231 and DESC0018192, as well as by an LDRD at Berkeley Lab.

REFERENCES

[1] Esarey, E., Schroeder, C. B., and Leemans, W. P., "Physics of laser-driven plasma-based electron accelerators," *Rev. Mod. Phys.* **81**, 1229–1285 (July–September 2009).

[2] Esarey, E., Shadwick, B. A., Catravas, P., and Leemans, W. P., "Synchrotron radiation from electron beams in plasma-focusing channels," *Phys. Rev. E* **65**, 056505 (May 2002).

[3] Rousse, A., Phuoc, K., Shah, R., Pukhov, A., Lefebvre, E., Malka, V., Kiselev, S., Burgy, F., Rousseau, J., Umstadter, D., and Hulin, D., "Production of a keV x-ray beam from synchrotron radiation in relativistic laser-plasma interaction," *Phys. Rev. Lett.* **93**(13), 135005 (2004).

[4] Ta Phuoc, K., Corde, S., Shah, R., Albert, F., Fitour, R., Rousseau, J.-P., Burgy, F., Mercier, B., and Rousse, A., "Imaging electron trajectories in a laser-wakefield cavity using betatron x-ray radiation," *Phys. Rev. Lett.* **97**, 225002 (November 2006).

[5] Kneip, S., Nagel, S. R., Bellei, C., Bourgeois, N., Dangor, A. E., Gopal, A., Heathcote, R., Mangles, S. P. D., Marqu/'es, J. R., Maksimchuk, A., Nilson, P. M., Phuoc, K. T., Reed, S., Tzoufras, M., Tsung, F. S., Willingale, L., Mori, W. B., Rousse, A., Krushelnick, K., and Najmudin, Z., "Observation of synchrotron radiation from electrons accelerated in a petawatt-laser-generated plasma cavity," *Phys. Rev. Lett.* **100**, 105006 (2008).

[6] Plateau, G. R., Geddes, C. G. R., Thorn, D. B., Chen, M., Benedetti, C., Esarey, E., Gonsalves, A. J., Matlis, N. H., Nakamura, K., Schroeder, C. B., Shiraishi, S., Sokollik, T., van Tilborg, J., Cs. Tóth, Trotsenko, S., Kim, T. S., Battaglia, M., Stöhlker, T., and Leemans, W. P., "Low-emittance electron bunches from a laser-plasma accelerator measured using single-shot x-ray spectroscopy," *Phys. Rev. Lett.* **109**, 064802 (2012).

[7] Schnell, M., Sävert, A., Landgraf, B., Reuter, M., Nicolai, M., Jäckel, O., Peth, C., Thiele, T., Jansen, O., Pukhov, A., Willi, O., Kaluza, M. C., and Spielmann, C., "Deducing the electron-beam diameter in a laser-plasma accelerator using x-ray betatron radiation," *Phys. Rev. Lett.* **108**, 075001 (2012).

[8] Wenz, J., Schleede, S., Khrennikov, K., Bech, M., Thibault, P., Heigoldt, M., Pfeiffer, F., and Karsch, S., "Quantitative x-ray phase-contrast microtomography from a compact laser-driven betatron source," *Nat. Comm.* **6**, 7568 (2015).

[9] Cole, J. M., Symes, D. R., Lopes, N. C., Wood, J. C., Poder, K., Alatabi, S., Botchway, S. W., Foster, P. S., Gratton, S., Johnson, S., Kamperidis, C., Kononenko, O., Lazzari, M. D., Palmer, C. A. J., Rusby, D., Sanderson, J., Sandholzer, M., Sarri, G., Szoke-Kovacs, Z., Teboul, L., Thompson, J. M., Warwick, J. R., Westerberg, H., Hill, M. A., Norris, D. P., Mangles, S. P. D., and Najmudin, Z., "High-resolution μct of a mouse embryo using a compact laser-driven x-ray betatron source," *Proc. Natl. Acad. Sci. USA* **115**, 6335 (2018).

[10] Guo, B., Zhang, X., Zhang, J., Hua, J., Pai, C.-H., Zhang, C., Chu, H.-H., Mori, W., Joshi, C., Wang, J., and Lu, W., "High-resolution phase-contrast imaging of biological specimens using a stable betatron x-ray source in the multiple-exposure mode," *Sci. Rep.* **9**, 7796 (2019).

[11] Hussein, A. E., Senabulya, N., Ma, Y., Streeter, M. J. V., Kettle, B., Dann, S. J. D., Albert, F., Bourgeois, N., Cipiccia, S., Cole, J. M., Finlay, O., Gerstmayr, E., Gonzalez, I. G., Higginbotham, A., Jaroszynski, D. A., Falk, K., Krushelnick, K., Lemos, N., Lopes, N. C., Lumsdon, C., Lundh, O., Mangles, S. P. D., Najmudin, Z., Rajeev, P. P., Schleputz, C. M., Shahzad, M., Smid, M., Spesyvtsev, R., Symes, D. R., Veux, G., Willingale, L., Wood, J. C., Shahani, A. J., and Thomas, A. G. R., "Laser-wakefield accelerators for high-resolution x-ray imaging of complex microstructures," *Sci. Rep.* **9**, 3249 (2019).

[12] Weingartner, R., Raith, S., Popp, A., Chou, S., Wenz, J., Khrennikov, K., Heigoldt, M., Maier, A. R., Kajumba, N., Fuchs, M., Zeitler, B., Krausz, F., Karsch, S., and Grüner, F., "Ultralow emittance electron beams from a laser-wakefield accelerator," *Phys. Rev. ST Accel. Beams* **15**, 111302 (2012).

[13] Yu, L.-L., Esarey, E., Schroeder, C. B., Vay, J.-L., Benedetti, C., Geddes, C. G. R., Chen, M., and Leemans, W. P., "Two-color laser-ionization injection," *Phys. Rev. Lett.* **112**, 125001 (2014).

[14] Mayo, S. C., Miller, P. R., Wilkins, S. W., Davis, T. J., Gao, D., Gureyev, T. E., Paganin, D., Parry, D. J., Pogany, A., and Stevenson, A. W., "Quantitative x-ray projection microscopy: phase-contrast and multi-spectral imaging," *J. Microscopy* **207**, 79 (2002).

[15] Schwoerer, H., Liesfeld, B., Schlenvoigt, H.-P., Amthor, K.-U., and Sauerbrey, R., "Thomson-backscattered x rays from laser-accelerated electrons," *Phys. Rev. Lett.* **96**, 014802 (2006).

[16] Phuoc, K. T., Corde, S., Thaury, C., Malka, V., Tafzi, A., Goddet, J. P., Shah, R. C., Sebban, S., and Rousse, A., "All-optical compton gamma-ray source," *Nat. Phot.* **6**, 308 (2012).

[17] Khrennikov, K., Wenz, J., Buck, A., Xu, J., Heigoldt, M., Veisz, L., and Karsch, S., "Tunable all-optical quasimonochromatic thomson x-ray source in the nonlinear regime," *Phys. Rev. Lett.* **114**, 195003 (2015).

[18] Golovin, G., Banerjee, S., Liu, C., Chen, S., Zhang, J., Zhao, B., Zhang, P., Veale, M., Wilson, M., Seller, P., and Umstadter, D., "Intrinsic beam emittance of laseraccelerated electrons measured by x-ray spectroscopic imaging," *Sci. Rep.* **6**, 24622 (2016).

[19] Pogany, A., Gao, D., and Wilkins, S. W., "Contrast and resolution in imaging with a microfocus x-ray source," *Rev. Sci. Instrum.* **68**, 2774 (1998).

[20] Huang, J. Y., Jin, K. S., Lim, J. H., Kim, H. Y., Jang, S. D., Choi, H. J., Gil, K. H., and Lee, S. K., "High resolution and high contrast bio-medical x-ray imaging technique using synchrotron radiation in pls," *J. Korean Phy. Soc.* **56**, 2077 (2010).

[21] D. Bleiner, The Science and Technology of X-ray Lasers: A 2020 Update Proc. SPIE 11886, 1188602 (2021)